Parts-per-Million Detection of Volatile Organic Compounds via Surface Plasmon Polaritons and Nanometer-Thick Metal–Organic Framework Films

Max L. Tietze,* Martin Obst, Giel Arnauts, Nathalie Wauteraerts, Sabina Rodríguez-Hermida, and Rob Ameloot*

ABSTRACT: Because of their guest adsorption properties, metal–organic frameworks (MOFs) are promising materials to realize chemical sensors. However, achieving high sensitivities requires the reproducible deposition of well-defined MOF films and their integration with a suitable sensor design. In this work, we report the sensitive detection of volatile organic compounds (VOCs) by transducing the adsorption in zeolitic imidazolate framework 8 (ZIF-8) thin films, prepared by chemical vapor deposition (MOF-CVD), into surface plasmon polariton (SPP) shifts measured via total internal reflection ellipsometry (TIRE). It is shown that defect formation during MOF-CVD alters the VOC uptake. However, SPP resonances tunable over the entire Vis–NIR range and as sharp as 14 nm are obtained for optimized synthesis conditions. Record-breaking shifts stronger than 150 nm upon methanol uptake and a limit of detection below 1 ppm are observed. By modeling the TIRE spectra, changes in the ZIF-8 refractive index from 1×10^{-4} (single-digit ppm VOC concentration) up to 0.06 are resolved with a resolution better than 1×10^{-5}.

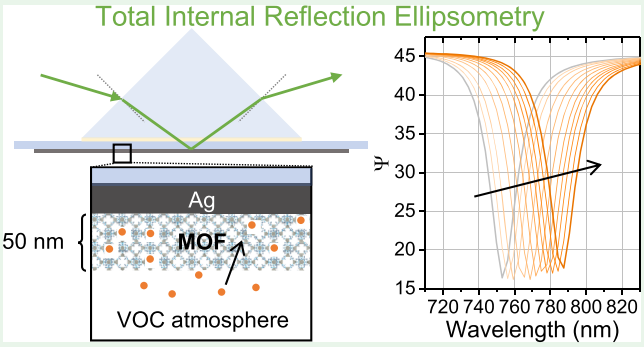

KEYWORDS: *metal–organic frameworks (MOFs), gas sensing, surface plasmon polariton (SPP), spectroscopic ellipsometry (SE), total internal reflection ellipsometry (TIRE)*

Sensing volatile organic compounds (VOCs) is important in various applications, e.g., in monitoring industrial processes and air quality or the detection of biomarkers in breath.[1] State-of-the-art miniature VOC sensors are based on semiconducting metal oxide (SMOx) thick-film chemiresistors. While these sensors can have low detection limits,[2] they lack selectivity.[3] Therefore, using porous materials with selective adsorption properties is an interesting alternative.[4,5] In particular, microporous metal–organic frameworks (MOFs) have gained interest due to their high internal surface areas and functionalizable pore interiors,[6] resulting in VOC uptake[7] even at trace levels in ambient conditions.[8,9]

Various sensor concepts have been developed to transduce the guest uptake in MOFs into a readable signal.[10] Optical sensors possess the advantage of a cheap readout, e.g., via a simple photodiode. In the simplest form of an optical sensor, the MOF itself indicates guest adsorption via a change of its color, i.e., its spectral absorption.[11] Also, changes in an MOF's photoluminescence spectrum were shown to indicate the adsorption of guests in the case of specific interactions between the framework and, for example, differently substituted aromatic guest molecules.[12] However, a broadly applicable sensing technology would employ a transduction principle that functions irrespective of the host–guest combination. Therefore, most optical sensor designs make use of an increase in the MOF's refractive index (n) upon guest adsorption.[13] This effect can be monitored either by scientific instruments such as ellipsometric porosimetry (EP) setups[13,14] or in integrated sensor designs. A selection of related sensor concepts is given in Table S1. A first class of devices represents Fabry–Perot interferometers[15] and oscillators for which VOC adsorption causes shifts in their optical resonance peaks. For instance, a shift of 340 pm was reported for a 121 pm sharp resonance of an 80 μm ring oscillator surrounded by a 1 μm coating of zeolitic imidazolate framework 8 (ZIF-8).[16] Fabry–Perot etalons employing ZIF-8 showed optical shifts of ca. 50–60 nm at a bandwidth of >100 nm.[17] The second type of devices, photonic crystals, employ MOFs in periodic structures with

alternating regions of low and high refractive indices, e.g., layered 1D distributed Bragg reflectors (DBRs)[18−22] or superlattices of MOF particles.[23] Light waves entering the photonic crystal undergo multiple reflections and destructive interference, which prevents their propagation at certain wavelengths, called stopbands. The spectral shift of a DBR stopband upon VOC adsorption is typically in the order of 30−50 nm,[18−21] exceptionally 100 nm.[22] To obtain the sharp stopband edges required for a high sensitivity, stacks of at least 3−5 bilayers are needed. The third sensor class employs plasmonics, either as localized surface plasmon resonances (LSPR) in metal nanoscale structures or nanoparticles[24] or SPR in metal films,[25,26] each in contact with an MOF coating. Broad plasmonic absorptions are typically observed (FWHM > 100 nm). SPR shifts upon guest adsorption in the MOF have been measured up to 75 nm.[25] LSPR spectral shifts are much weaker and more difficult to control.[24]

The signal (S) in the sensor concepts described above is typically the transmitted or reflected light intensity, which in the simplest case is monitored at a single wavelength. Therefore, both the sensitivity ($\Delta S/\Delta c$, with c being the VOC concentration in the atmosphere) and the lower limit of detection (LoD) are determined by the attainable shift of spectral features ($\Delta\lambda/\Delta n$) versus the "sharpness" of these features (expressed, e.g., as the full width at half maximum, FWHM). In most reported sensor designs, the largest shift $\Delta\lambda_{max}$ upon VOC adsorption is similar or even lower than the width of their spectral features, which limits sensitivity. The sensitivity $\Delta S/\Delta c$ is further governed by the VOC uptake in the MOF, as this directly determines $\Delta n/\Delta c$. The adsorption of VOCs into microporous MOFs is typically nonlinear (e.g., type I or sigmoidal adsorption isotherms). For ZIFs, the step in the sigmoidal isotherm appears at rather high concentrations (>1000 ppm) and is typically sharper for more polar VOCs.[27] To resolve uptake in the application-relevant ppm range or even below,[4] it is hence desired to explore optical sensor designs in which both the transduction mechanism $\Delta\lambda/\Delta n$ and the $\Delta\lambda_{max}$/FWHM ratio of the sensor's spectral feature are maximal. This way, even very small changes in Δn can be detected, enabling a very low LoD.

In this work, we demonstrate for the first time the highly sensitive transduction of VOC uptake in MOF thin films into surface plasmon polariton (SPP) shifts by applying spectroscopic total internal reflection ellipsometry (TIRE). SPP resonances as sharp as 14 nm and tunable over the entire Vis−NIR range are obtained for ZIF-8 thin films deposited on metal-coated glass by chemical vapor deposition (MOF-CVD).[28] Upon VOC adsorption, optical shifts of up to 160 nm and an LoD of <1 ppm are demonstrated. Optical modeling enables resolving changes in the MOF refractive index by less than 1×10^{-5} refractive index units (RIUs), thus outperforming conventional ellipsometric porosimetry. The FWHMs of the SPP resonances are shown to correlate with the roughness of the MOF films. Therefore, a very high MOF film quality is required to make full use of the ultrahigh sensitivity of this transduction mechanism. These findings will be very helpful for the future development of microintegrated MOF-based optical gas sensor arrays with a very high sensitivity.

■ RESULTS AND DISCUSSION

Sensing Principle. SPP excitation is suitable to characterize adsorption phenomena with high accuracy.[29] For instance, it has been used to detect DNA monolayers on CrAu films.[30] Also, VOC sensing via absorption into nonporous polymers has been shown.[31] The TIRE sample configuration is shown in Figure 1a. Incident linearly p- and s-polarized light is coupled

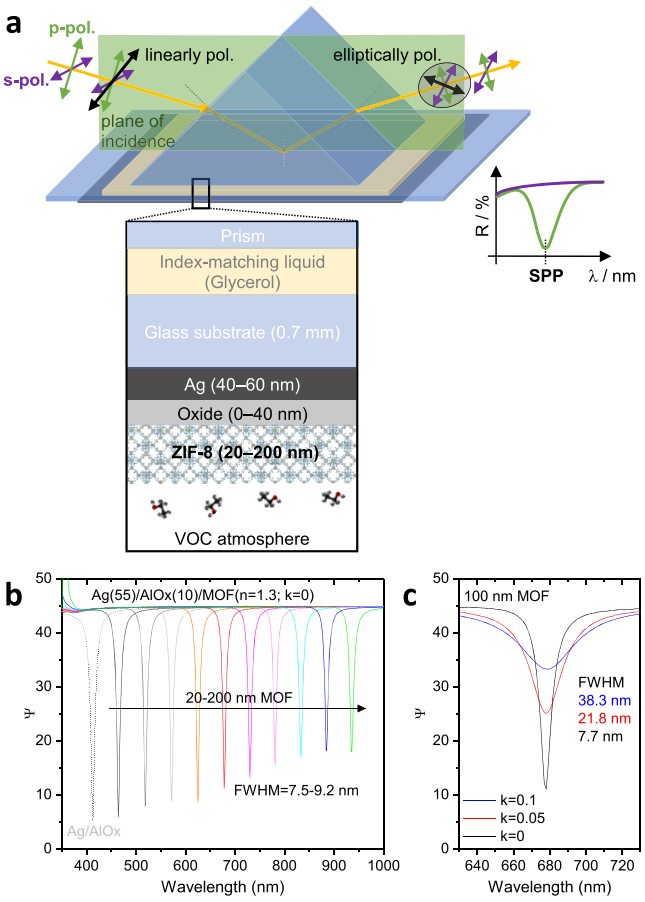

Figure 1. TIRE/SPP principle. (a) TIRE measurement geometry and sample layer stack. (b) Modeled SPP spectra for Ag(55 nm)/AlOx(10 nm)/MOF stacks with MOF layers in the 20−200 nm thickness range. (c) Modeled SPP broadening due to an increase in the MOF k-value from 0 to 0.1 for a 100 nm MOF film.

into a glass substrate via a right-angle prism and totally reflected at its backside, which is coated with a metal thin film (Kretschmann geometry). As a result, SPP waves are excited in the metal film via coupling to the p-polarized light. Since Ψ in spectroscopic ellipsometry (SE) is related to changes in the amplitude ratio of p- and s-polarized light,[32] a drop in Ψ is a direct measure for the strength of the SPP excitation. The SPP frequency ω_{SP} is determined by the metal plasma frequency ω_P and the complex dielectric function $\underline{\varepsilon}_d = \underline{n}_d^2 = (n_d + i\kappa_d)^2$ of the surrounding medium, with n_d and κ_d denoting the dielectric's refractive index and extinction coefficient, respectively, via eq 1.[33]

$$\omega_{SP} = \omega_P \Big/ \sqrt{1 + \underline{\varepsilon}_d} \tag{1}$$

The SPP frequency ω_{SP} (or resonance wavelength λ_r) is sensitive to $\underline{\varepsilon}_d$ of the surrounding medium up to a few hundreds of nm away from the metal surface, and ω_{SP} decreases (λ_r increases) when $\underline{\varepsilon}_d$ increases.

In this work, layered samples of the type Ag/oxide/MOF deposited on a glass substrate are investigated. To illustrate the SPP shift with rising thickness of the MOF film, optical

modeling is performed on Ag(55 nm)/AlOx(10 nm)/MOF stacks. For the sake of simplicity, the MOF film is described by a nondispersive Cauchy model (n = 1.3, k = 0) and the AlOx layer by n and k database values (CompleteEASE, Cauchy model). For the Ag layer, optical constants determined via spectroscopic ellipsometry (SE) in conjunction with transmission measurements on glass/Ag samples are applied. A detailed characterization of the optical properties and morphology of the RF-sputtered Ag films used throughout this work is given in Figure S1. For bare Ag films, the TIRE spectra show Ψ peaks at 370 nm (FWHM = 16.4 nm). Adding 10 nm AlOx shifts the SPP just beyond 400 nm (Figure 1b). Adding 20−200 nm of MOF on top yields SPP peak positions from 464−935 nm, with FWHMs of 7.5−9.2 nm. Since MOF materials may not be ideally transparent (k > 0) and can even undergo spectral absorption (color) changes upon adsorption or desorption of guest molecules,[11] the impact of k on the SPP peak is illustrated in Figure 1c. As shown for a 100 nm MOF film, an increase of k from 0 to 0.1 broadens the SPP FWHM to almost 40 nm without altering its position.

As shown in Figure 2a, the SPP λ_r linearly correlates with the thickness of the MOF layer (t_{MOF}), and the slope increases

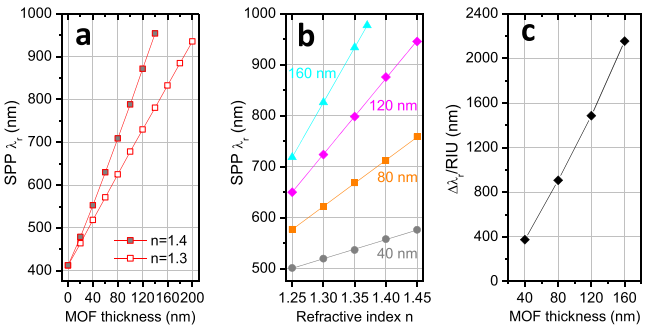

Figure 2. Sensitivity analysis. SPP peak positions λ_r modeled for Ag(55 nm)/AlOx(10 nm)/MOF(20−200 nm) stacks plotted vs (a) the MOF thickness or (b) the MOF refractive index. (c) Corresponding sensing sensitivity in terms of $\Delta\lambda_r$/RIU.

with its refractive index (plotted for n = 1.3 and 1.4). Thus, the SPP shift $\Delta\lambda_r$ for the same refractive index change Δn is higher for thicker MOF films. As illustrated in Figure 2b, SPP λ_r correlates linearly with the refractive index n, and the slope $\Delta\lambda_r/\Delta n$ is steeper for thicker MOF films. The sensitivity of the SPP/MOF configuration in terms of SPP shift per change in refractive index unit, $\Delta\lambda_r$/RIU, is given in Figure 2c. For a 40 nm MOF coating, it is 380 nm/RIU and increases approximately linearly to 2150 nm/RIU for a 160 nm MOF layer. Typically, the maximal Δn in MOFs upon VOC uptake (i.e., Δn for high pore filling w.r.t. to the activated material) is of the order of 0.1.[13] An MOF-based sensor in the TIRE configuration with $\Delta\lambda_r$/RIU of 1000 would thus yield an SPP peak shift of 100 nm, which is considerably more than most of the reported values (Table S1) and can be realized with an MOF film only 85−90 nm thin (cf. Figure 2c).

The LoD and sensitivity of a practical SPP/MOF sensor, i.e., in which changes in the reflected light intensity (ΔI_R) are monitored, is further determined by the FWHM of the SPP peak since small shifts are more readily detected for sharp peaks. As illustrated in Figure 1c, the MOF layer's k-value crucially determines the SPP FWHM. Therefore, to obtain a high sensitivity $\Delta I_R/\Delta c$, MOF films with weak optical absorption ($k \ll 0.1$) and high uptake ($\Delta n/\Delta c$) are required. In the following sections, it is shown that MOF-CVD ZIF-8 films with t_{MOF} <120 nm can fulfill these requirements, yielding an LoD of <1 ppm for methanol vapor.

Optimization of the MOF-CVD ZIF-8 Thin Film Growth. Throughout this work, ZIF-8 films are synthesized in a Schlenk tube via MOF-CVD starting from RF-sputtered ZnO precursor films on 54 mm × 54 mm Ag(50 nm)/AlOx(10 nm)-coated glass substrates. First, the conversion of 6 nm ZnO is studied in detail. The ZIF-8 thickness as a function of the conversion time shows an S-shaped increase until full conversion is reached after 18 h (Figure 3a; corresponding SE spectra are given in Figure S2a). The resulting TIRE spectra (Figure 3b) show an increasing SPP redshift with increasing conversion time. AFM images of the samples are given in Figure 3c, and the RMS roughness and the corresponding SPP FWHMs are plotted as a function of conversion time in Figure 3d. Both parameters increase with increasing ZIF-8 thickness, with a sharp rise around 12 h of conversion, i.e., where the thickness expansion is fastest (cf. Figure 3a). The fully converted films show an RMS roughness of >20 nm and 35 nm wide SPP peaks, whereas ZIF-8 films thinner than 80 nm yield SPP resonances as sharp as 14 nm and a roughness in the order of only 10 nm. As the roughness increases, the appearance of the samples changes from highly reflecting mirror-like toward more dull and green-beige tinted (Figure S2b). As the observed color does not change with the viewing angle, it is attributed to light scattering rather than thin film interference (ZIF-8 is expected to be transparent in the visible range as an electronic band gap of 5 eV was estimated by DFT[34]). The GIXRD diffractograms of the 15 and 18 h samples, each activated at 110 °C for 4 h in ambient air, show the characteristic diffractions of ZIF-8 (Figure 3e), with the three main peaks at 7.5 [110], 10.7 [200], and 13.0° 2θ [211]. Compared to previously simulated and measured MOF-CVD ZIF-8 diffractograms,[35] the [200] diffraction is enhanced w.r.t. to the [110] and [211] diffractions, particularly for the 18 h sample, which might be attributed to a slightly preferential [100] orientation.[36,37] Also, the [110]/[211] diffraction intensity ratio is <1 for the 18 h sample, whereas for the 15 h sample, it is >1. Upon activation, the [110] diffraction intensity is expected to increase in intensity due to desorption of unreacted linkers from the pores (see Figure S3a). Since this is not the case for the 18 h film, we conclude that it does not properly activate.

To study the film porosity, the SPP redshift upon methanol (MeOH) adsorption is monitored as a function of concentration (Figure 3f,g). The 12 and 15 h samples, designated as "S6a" and "S6b", show an S-shaped isotherm similar to previously reported ZIF-8 films.[27] At p/p^0 = 70%, $\Delta\lambda_r$ reaches almost 50 nm. The samples with longer conversion times, however, show lower MeOH uptake ($\Delta\lambda_r$ = 20−30 nm for p/p^0 = 70%), even when the activation procedure is increased to 8 h or performed in a vacuum (Figure S3b). Although the ZIF-8 film thickness does not substantially increase after 15 h of conversion (110 nm vs 90 nm; Figure 3a), the samples obtained after longer conversion times show significantly redshifted SPP peaks (Figure 3b; λ_r = 700−750 nm), i.e., their refractive index must be higher. Similar results are obtained for ZIF-8 films synthesized from only 5 or 4 nm ZnO, resulting in optimal MOF-CVD times in terms of sensing response of 8.5 and 6 h, respectively (Figures S3c,d). The optimal MOF-CVD conversion time correlates approximately linearly with the

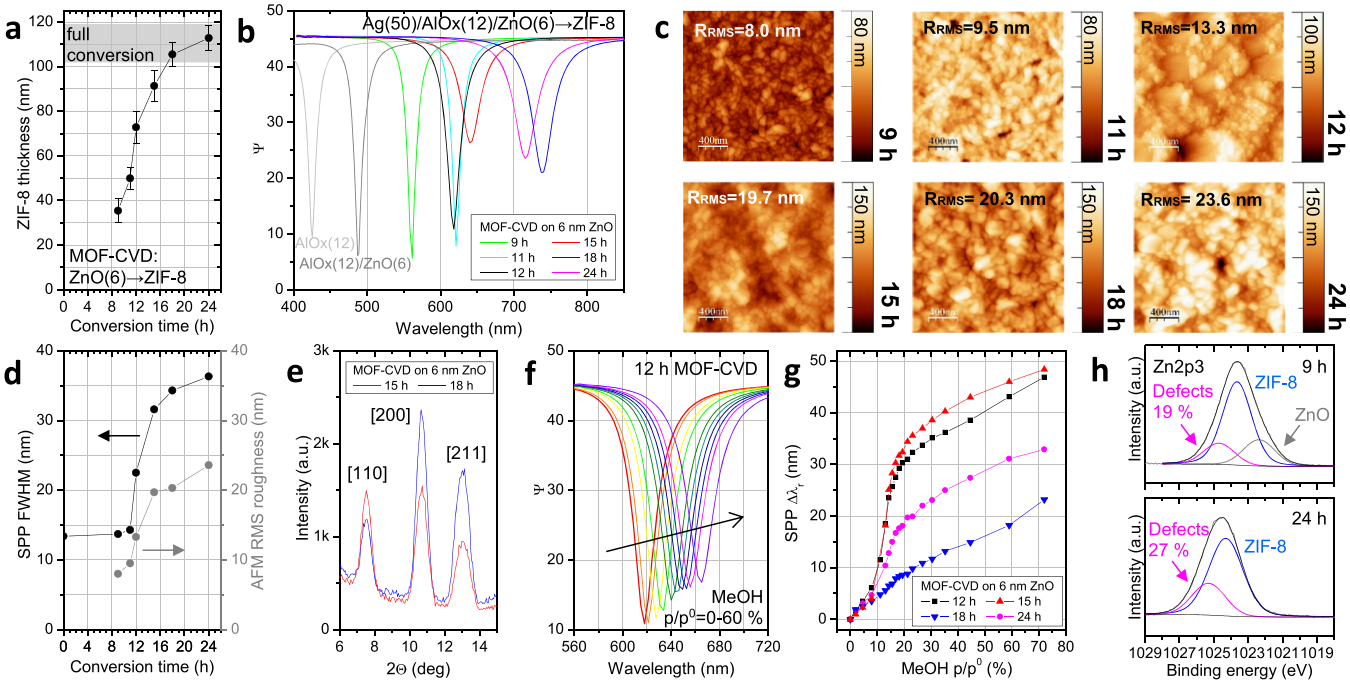

Figure 3. Characterization of Ag/AlOx/ZIF-8 SPP samples with MOF-CVD ZIF-8 grown from 6 nm ZnO. Evolution of the ZIF-8 thickness (a) and SPP peak positions of samples (b) with increasing conversion time. (c) Corresponding AFM images. (d) Evolution of the SPP peak FWHMs and AFM RMS roughness with the conversion time. (e) GIXRD diffractograms of samples converted for 15 and 18 h. (f) Illustration of the SPP redshift upon exposure to MeOH vapors in the concentration range p/p^0 = 0−60%. (g) Corresponding sensing characteristics $\Delta\lambda_r(p/p^0)$ determined on samples of varying conversion time. (h) Zn 2p3 core-level HAXPES spectra of Si/ZIF-8 samples with a semiconverted (9 h MOF-CVD, upper panel) and a fully converted ZIF-8 film (24 h MOF-CVD, lower panel).

ZnO precursor thickness (Figure S3f). Keeping the fully converted ZIF-8 films for longer in the saturated 2-methylimidazole (2-mIm) atmosphere seems to cause structural changes, as indicated by the reduced intensity of the [110] diffractions (cf. Figure 3e and Figure S3e) and a lower MeOH uptake. Since no new diffractions are observed in GIXRD, we presume that the SOD topology is maintained and rather than inducing a transition to a denser phase,[38] the prolonged 2-mIm exposure likely introduces defects in the lattice.

Brief Discussion on Defects. To gain a deeper insight into the composition of the ZIF-8 films and understand the origin of reduced VOC uptakes at long conversion times, hard X-ray photoemission spectroscopy (HAXPES) measurements are performed on films grown on silicon. Since the inelastic mean free path of photoelectrons in HAXPES using Ga K_α irradiation ($h\nu$ = 9.52 keV) is several times larger than in Al K_α XPS,[39] the bulk properties rather than the surface properties of the ZIF-8 thin films are probed in these measurements. Two ZIF-8 samples, obtained after 9 and 24 h conversion of 6 nm ZnO, are investigated. After 24 h of linker exposure, a 100 nm film is obtained (full conversion), with a refractive index (at 632.8 nm) as high as 1.4662 (1.4149) before (after) activation (Table S2 and Figure S4a). On the contrary, 9 h of MOF-CVD yields a film of only 59 nm with a lower refractive index of 1.3582 after activation. Similar to the SPP samples, the 24 h MOF-CVD film on silicon also shows a [110]/[211] ratio of <1 in GIXRD, whereas for the 9 h film, it is >1 (Figure S4b). HAXPES survey scans reveal clear C 1s, N 1s, and Zn 2p signals (Figure S4c,d). Furthermore, small but visible O 1s as well as Si 1s signals (including Si plasmonic excitations) are present. The latter originate from the Si substrate underneath the MOF films. High-resolution scans of Zn 2p3 indicate the formation of ZIF-8 with two main subpeaks (Figure 3h). The 9 h sample additionally shows as a subpeak related to unconverted ZnO (1022.2 eV) as concluded by comparison to the spectra of a Si/ZnO(6.1 nm) reference sample (Figure S4e). The main peak in the Zn 2p3 signal (marked blue, 1023.7 eV) is attributed to intact ZIF-8, i.e., Zn atoms coordinated to four 2-mIm linkers, whereas the high-binding-energy shoulder (marked magenta, 1024.7 eV) likely corresponds to defective ZIF-8. The same is observed in the N 1s signals (Figure S4c,d), and the defect fractions account for 16−19% (27−32%) in the 9 h (24 h) CVD sample. We think that this high fraction of defects in the 24 h CVD sample is responsible for the reduced MeOH uptake observed in films obtained at reaction times longer than optimal (cf. Figure 3g).

Zn^{2+} vacancies, linker vacancies (Zn-X···H_2O-Zn), and dangling linkers (Zn-X···HmIm-Zn) in which X is OH^-, NO_3^-, or $COOH^-$ have been discussed as defects in ZIF-8.[40] Also the formation of carbonate complexes in the presence of humidified CO_2 was reported for ZIF-8.[46] In fact, the N/Zn ratios for the 9 and 24 h samples are 3.2 and 3.3, respectively. Therefore, both films contain less 2-mIm than expected based on the structure formula ($C_8H_{10}N_4Zn$). Furthermore, the O/Zn ratio is as high as 0.7 for both samples, whereas no oxygen is expected in defect-free ZIF-8. The O 1s signals of the two samples contain two subpeaks (Figure S4c,d): 533.5 eV (marked orange) and 534.8 eV (marked red), which are assigned to oxygen-containing species bound to defects in the framework, e.g., OH (orange peak) or H_2O or/and CO3 (red peak) groups.[41] Consistently, a small high-binding energy subpeak (289.9 eV) is observed in the C 1s scans, comparing well to C 1s reported for $ZnCO_3$.[41] The FWHMs of the two main ZIF-8-related C 1s peaks are broader by 0.2 eV in the 24

h sample than in the 9 h sample. Therefore, another subpeak related to defects such as dangling linkers is suspected there. A more detailed analysis goes beyond the scope of this article and will be discussed elsewhere.

It was further observed that semiconverted ZIF-8 films amorphized when stored in ambient air for several weeks, likely by breaking the Zn−mIm coordination bond in the presence of water vapor. However, a subsequent 2 h exposure to linker vapor yields highly crystalline films as shown in Figure S5a for a set of SPP samples with the ZIF-8 grown from 6 nm ZnO for 9, 11, or 15 h in the first step. The second 2 h step strongly redshifts the SPP peaks beyond 700 nm. At the same time, the peaks become substantially sharper (FWHM = 15−20 nm) than for samples fully converted in one step (cf. Figures S5b vs Figure 3b) due to the lower roughness of "two-step" films (15 nm vs 20−25 nm; Figure S5c vs Figure 3c). Consistently, their appearance is less dull and more reflective (cf. Figure S5d vs Figure S2b). MeOH uptake experiments yielded SPP shifts $\Delta\lambda_r$ as strong as 80 nm for the (11 + 2) h MOF-CVD sample (Figure S5e), which has a 116 nm ZIF-8 film and a sharp SPP peak (16.4 nm FWHM) and is now referred to as sample S6c. Its MeOH uptake is clearly higher than for samples with the same ZIF-8 thickness obtained from 6 nm ZnO in one step (cf. Figure 3a,g). We think that storage in ambient air does lead to protonation of linkers or/and the formation of -Zn-H_2O defects, which enables a (re)crystallization and defect healing in the second conversion step[35] by the incorporation of additional linkers. Control experiments (not shown here) revealed that ca. 3 weeks of storage in ambient air are needed for this two-step process.

SPP Samples with Varying ZIF-8 Thin Film Thicknesses. As shown in Figure 2c, the sensitivity scales with the MOF thickness. Therefore, a series of samples of the type Ag(40,50 nm)/ZnO(0, 15, and 30 nm)/AlOx(12 nm)/ZIF-8 was prepared via the conversion of 4−12 nm precursor ZnO films deposited on top of the AlOx layer. Upon conversion, a thicker ZnO precursor film will yield a thicker ZIF-8 film (see Figure 4a), with a theoretical thickness expansion by a factor of 16−17 for full conversion of crystalline ZnO.[28] A second ZnO film, underneath the AlOx layer and not converted to ZIF-8, is included as an optical spacer to demonstrate SPP λ_r tuning for samples with very thin ZIF-8 films. The samples are named "S*x*_*y*", with *x* and *y* being the thicknesses of the ZnO precursor and optical spacer layers, respectively. An overview of the sample structures and MOF-CVD conversion times is given in Table 1. The ZIF-8 thickness ranged from 39.4 nm (S4) to 192 nm (S12) as obtained by modeling SE spectra (Figure S6 and Table S3). The TIRE spectra of the activated samples without spacer layers are shown in Figure 4b. The observed SPP peak position scales approximately linearly with the ZIF-8 thickness (Figure 4c), which means that the refractive index of the MOF film does not depend on its thickness (cf. Figure 2a). All samples show [110]/[211] diffraction peak intensity ratios of >1 in GIXRD (Figure S7a), confirming their porosity/activation. Practically identical diffraction patterns are obtained for the samples S4, S4_15, and S4_30 regardless of the ZnO spacer layer underneath, which confirms (1) the functionality of the AlOx layer as a 2-mIm barrier during MOF-CVD and (2) the reproducibility of the synthesis method. As illustrated in Figure S8, 6 h of MOF-CVD redshifts the SPP peaks by 160 ± 10 nm for each of these samples, which corresponds to the formation of 35−40 nm ZIF-8. AFM images of all samples are given in Figure S9a, and

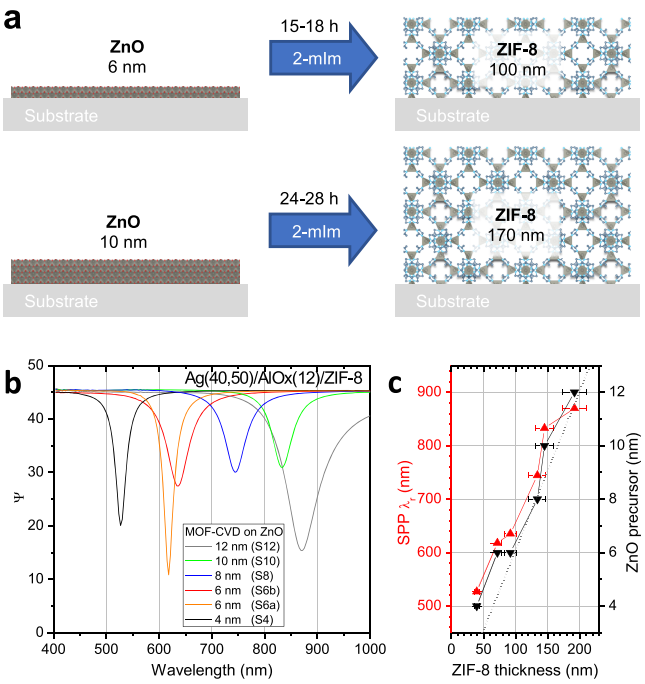

Figure 4. SPP properties of sample series S4−S12. (a) Illustration of the MOF-CVD process for obtaining ZIF-8 thin films of varying thicknesses. (b) TIRE spectra (incident angle of 70°) measured on Ag(50 and 40 nm)/AlOx(12 nm)/ZIF-8 samples, with the MOF obtained from 4−12 nm ZnO precursor thin films. (c) Corresponding SPP λ_r vs the ZIF-8 thickness fitted from SE (cf. Figure S6). The dotted line indicates the theoretical thickness expansion from crystalline ZnO to ZIF-8 (factor 17).

Table 1. Structure and SPP Properties of Samples S4−S12[a]

	S4	S4_s15	S4_s30	S6a	S6b	S8	S10	S12
Ag	50							40
ZnO	-	15	30	-	-	-	-	-
AlOx	12							-
ZnO	4			6		8	10	12
MOF-CVD	6 h			12 h	15 h	24 h	28 h	24 h
SPP λ_r @ 70°	527	633	759	618	635	745	833	870
FWHM	23.9	13.6	14.4	22.5	31.6	46.6	44.8	78.7
R_{RMS}	9.0	8.3	10.0	13.3	19.7	30.2	27.2	52.8

[a]Layer thickness, SPP λ_r, FWHM, and AFM RMS roughness values are given in nm.

the RMS roughness increases with increasing ZIF-8 thickness, from <10 nm for the S4 samples to >40 nm for sample S12. The same trend is found for the SPP FWHMs, which range from 14 nm to almost 80 nm. In Figure S7b, for all measurements performed in this work, the SPP FWHMs are plotted against the respective AFM RMS roughness, demonstrating a clear positive correlation. Also, an increase in the *k*-values (at 632.8 nm) from 0.00686 for very thin and smooth (S4) to 0.0472 for thick and rough (S12) ZIF-8 films was determined by SE modeling (Table S3).

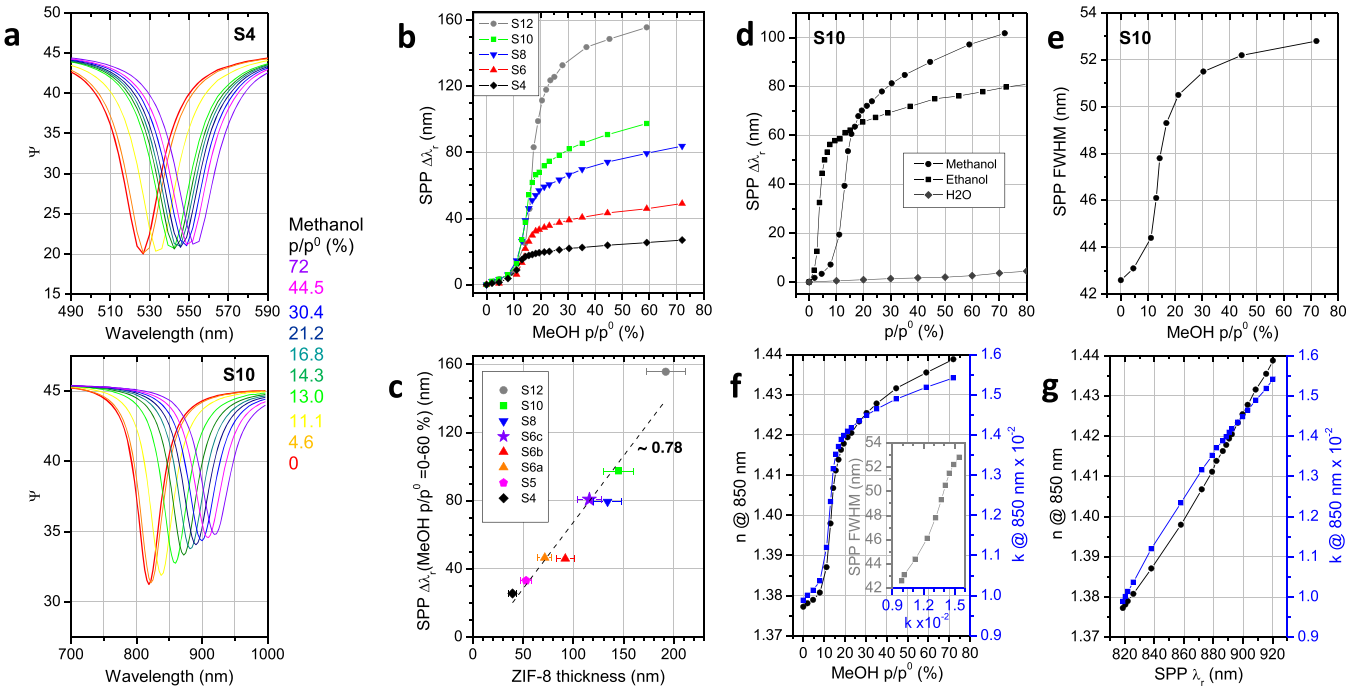

Figure 5. Sensing properties of series S4–S12. (a) TIRE spectra of samples S4 and S10 under exposure to dry MeOH vapor with p/p^0 = 0–72%. Spectra of the other samples are given in Figure S9. (b) Corresponding MeOH sensing characteristics $\Delta\lambda_r(p/p^0)$. (c) The samples' MeOH sensing strength (in terms of SPP $\Delta\lambda_r$ for p/p^0= 0–60%) plotted against their ZIF-8 film thickness, indicating a linear correlation, which is in agreement with Figure 2. (d) Sensing characteristics for ethanol and methanol in comparison to water, exemplarily measured on sample S10. (e) SPP FWHM vs MeOH p/p^0 for sample S10. Optical n and k values, determined from modeling the TIRE/SPP spectra of sample S10 vs (f) the MeOH partial pressure p/p^0 and (g) the SPP peak position λ_r. The time evolution of the modeled n and k values during the MeOH dosing is given in Figure S10d.

Sensing Performance. An analysis of the VOC sensing performance of the sample series S4–S12 is given in Figure 5, with the SPP peaks recorded during exposure to MeOH vapors at different p/p^0 shown in Figure 5a and S9b, respectively. Systematic and reversible redshifts of the SPP peaks are observed upon contact of the sensors with MeOH vapor. The plots of the $\Delta\lambda_r$ values as a function of the MeOH concentration (Figure 5b) closely resemble reported adsorption isotherms, for instance, for solvothermally grown ZIF-8 films.[27] Samples S4, S4_15, and S4_30, with 35–40 nm ZIF-8 each, show similar shifts of about 25 nm (Figure S9c). As expected from Figure 2b,c, samples with thicker ZIF-8 films yield stronger shifts, approaching 160 nm in the case of sample S12 with 192 nm ZIF-8. The response is so strong that the SPP peak moves out of the spectral range of the ellipsometer (>1000 nm). For all samples, the SPP shift for p/p^0 = 65% w.r.t. to the baseline in nitrogen is plotted vs the ZIF-8 thicknesses in Figure 5c, and a linear correlation with a slope of 0.78 nm/nm is found. Since λ_r generally scales linearly with both n and t_{MOF} (Figure 2), it can be concluded that the underlying Δn is approximately the same for all the samples, i.e., they are equally porous. Furthermore, the SPP peaks of S10 broaden with increasing VOC uptake (Figure 5a, bottom). A plot of the SPP FWHMs as a function of the MeOH concentration (Figure 5e) shows the same profile as the sigmoidal adsorption isotherm. For very thin films, i.e., those with small fitted k-values, the SPP broadening is less pronounced (see Figure 5a, top). Since the SPP FWHM correlates with the MOF k-value (Figure 1c and eq 1), these findings indicate that SPP-based sensing can resolve the presence of analytes in the MOF pores via changes in k as well.

The uptakes of ethanol (EtOH) and water vapor were evaluated for sample S10 (Figure 5d). At 70% relative humidity, the SPP redshifts only 3.6 nm w.r.t. to dry nitrogen, indicating the hydrophobicity of the ZIF-8 film. For EtOH and MeOH at relative vapor pressures of 70 %, however, the $\Delta\lambda_r$ reaches 80 and 102 nm, respectively. For p/p^0 < 15%, a significantly stronger uptake of EtOH than of MeOH is observed, as expected for ZIF-8.[27]

Optical Modeling and Comparison to Conventional Ellipsometric Porosimetry. In the following, the optical constants are determined via modeling the TIRE SPP sensing data and compared to ellipsometric porosimetry measurements (VOC uptake characterization via n and k modeling by fitting Ψ and Δ spectra in a conventional SE geometry). Optical modeling is performed first for sample S10 because (1) a clear interference maximum around 650 nm is observable in SE (Figure S10a), yielding a good fit, and (2) the SPP response, $\Delta\lambda_r$, is as strong as 100 nm while a clear broadening of the SPP excitation upon MeOH uptake is observed. The ZIF-8 film thickness is 144.4 nm. Details of the used SE model are given in Table S3. For TIRE modeling, an angle offset of −8.1° is used due to refraction at the Cathete edges of the right-angle prism (70° incident angle, n_{prism} = 1.455). The modeled refractive index (at 850 nm) of the ZIF-8 film after 2 h of activation is 1.3772 in a nitrogen atmosphere. MeOH uptake from vapors with p/p^0 of up to 72% increases n by up to 0.0616, reaching 1.4388. The refractive index plotted as a function of the MeOH concentration resembles the expected isotherm as for the SPP resonance λ_r (Figure 5f,d). The same holds for the extinction coefficient, k, which increases from 0.0099 to 0.0154. As shown in Figure 5g, the modeled n and k both follow a linear correlation with the SPP λ_r for different

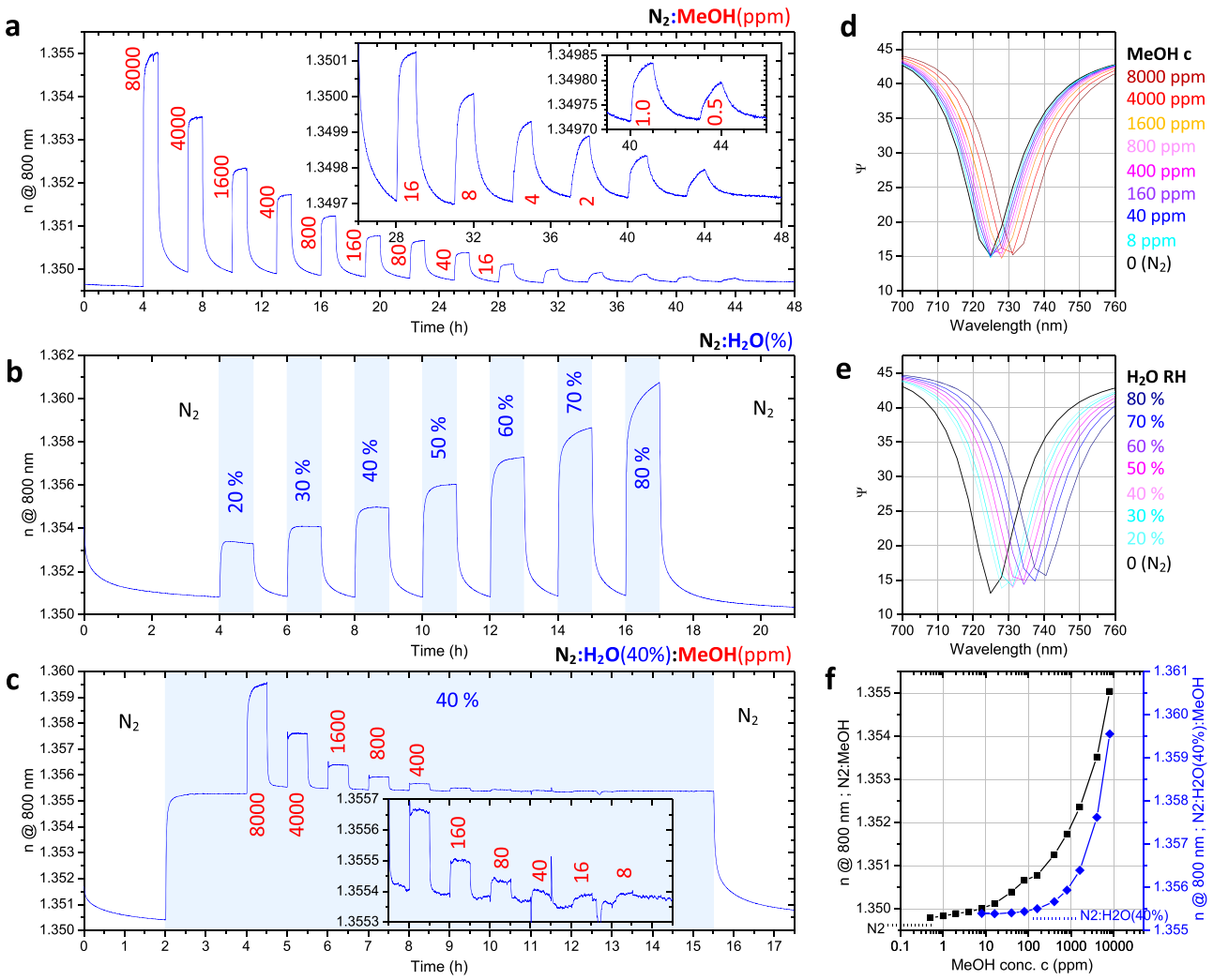

Figure 6. LoD of MeOH in dry and humidified nitrogen. Refractive index response of the ZIF-8 layer in sample S6c (cf. Figures S5 and S13) determined by modeling the SPP peak shifts during exposure to (a) MeOH in dry nitrogen, (b) nitrogen of varying relative humidity, and (c) MeOH in humidified nitrogen at a relative humidity of 40%. Red numbers indicate the MeOH concentration in ppm. The measured SPP peak redshifts are given in (d) and (e) as well as in Figure S13d. (f) Modeled refractive index values vs the MeOH concentration for MeOH pulses in dry nitrogen (left axis) or in humidified nitrogen (right axis). The dotted lines represent the baseline levels for each of the experiments.

MeOH concentrations, which indicates self-consistency of the fit because λ_r and n are expected to scale linearly based on theory (cf. Figure 2b).

Similar values and characteristics are obtained for a MeOH dosing experiment on the same sample but in a conventional SE configuration (Figure S10a−c). Here, an increase in n from 1.3700 in nitrogen to 1.4336 at p/p^0 = 59% is determined for the ZIF-8 layer. The increase of Δn = 0.0636 is similar to the value modeled for the TIRE geometry. However, although the fitting error is significantly lower in SE (root mean squared error (RMSE) of <3 vs >10 for SPP spectra), the fluctuation of the modeled optical constants, particularly in the extinction coefficient, is clearly larger in SE (cf. Figure S10d,c). The reason is that n is directly correlated with the SPP λ_r position and k is directly correlated with its FWHM, whereas SE requires fitting of the entire Ψ and Δ spectra to determine n and k, which renders the former method more precise with regard to resolving relative changes. This difference becomes particularly clear for very thin MOF films, which do not show a clear interference maximum in SE but have a sharp SPP peak due to their low roughness. For instance, for a Ag(50 nm)/AlOx(24 nm)/ZnO(4 nm) sample for which the ZnO layer is converted to 34.4 nm of ZIF-8 (6 h MOF-CVD), the change in refractive index is modeled with much lower noise in the TIRE configuration than in the SE configuration (Figure S11). For the latter, the noise is ca. 0.002 RIU, whereas for the former, it is $<10^{-4}$. These values show the potential of SPP-based gas sensing via MOFs in accurately resolving very small changes in the uptake of VOCs.

LoD in Dry and Humidified Nitrogen. The high sensitivity of the SPP approach is expected to translate into a low LoD. To resolve the MeOH uptake in the ppm range, samples with sharp resonances are required, i.e., for which the $\Delta\lambda_r$/FWHM ratio is as high as possible while ideally possessing a thick MOF film (Figure 2b,c). However, it was observed that samples with ZIF-8 films with thicknesses greater than 100 nm show rather broad SPP peaks due to their increased roughness (Table 1 and Table S3). This effect even holds for ZIF-8 films obtained from converting only 6 nm ZnO, marking the transition from sharp to broad SPP peaks when approaching full conversion (samples S6a vs S6b). Therefore, the $\Delta\lambda_r(p/p^0$ = 0−60% MeOH)/FWHM values of all samples of the series S4−S12 are

compared in Figure S12a, including a sample with the ZIF-8 grown by the conversion of 5 nm ZnO (S5_24). Values between 1.46 (S6b) and 2.17 (S10) are found. For sample S6c grown via two MOF-CVD steps, a substantially higher $\Delta\lambda_r$/FWHM of 4.87 is observed. Therefore, LOD measurements are performed on S6c and compared to S5_24 as the latter shows an equally sharp SPP (FWHM = 17.7 nm) at a reasonably high $\Delta\lambda_r$/FWHM of 1.89.

Sample S5_24 has the structure Ag(50 nm)/ZnO(24 nm)/AlOx(12 nm)/ZIF-8(50 nm) and shows a sharp SPP peak at 754.0 nm, which redshifts by 33.1 nm upon MeOH uptake at p/p^0 = 65% (Figure S12b). For p/p^0 = 10% (ca. 16,000 ppm), $\Delta\lambda_r$ is only 5.1 nm. To resolve uptake at even lower concentrations, Ψ at a fixed wavelength a few nm lower than the baseline λ_r (in dry nitrogen) is defined as sensor signal, i.e., Ψ(746.8 nm). An LoD as low as 20 ppm (Figure S12c) can be reached because the Ψ readout is positioned at the edge of the very sharp SPP peak, i.e., where $d\Psi/d\lambda$ is maximal. It is remarkable that MeOH uptake down to the a few tens of ppm can be resolved despite using only a few 10 nm thin ZIF-8 films. QCM-based VOC sensors based on solvothermal ZIF-8 films a few 100 nm to 1 μm thick could resolve uptake only down to 1000 ppm,[27] and other optical sensing techniques can typically resolve uptake down to a few hundreds of ppm.[26] LoD values of <1 ppm or even <100 ppb have been reported only rarely.[16]

If the MOF-CVD ZIF-8 adsorbs MeOH in the single-digit ppm range, it might be possible to resolve that via sample S6c. This sample has been repeatedly activated for at least 1 h at 110 °C under nitrogen flow before transferring it to the ellipsometer, where it was purged with dry nitrogen for several hours to entirely desorb residual water. Consecutively, three sensing runs were performed with pulses of: (1) MeOH (8000 to 0.5 ppm) in dry nitrogen, (2) nitrogen with a relative humidity of 20 to 80%, and (3) MeOH (8000 to 8 ppm) in nitrogen at 40% relative humidity. The baseline SPP positions before each of these runs were near-identical (724.5−725.7 nm). The equilibrium SPP peak positions, the Ψ readouts (at a suitable wavelength), and the modeled ZIF-8 refractive index for each of the three experiments are given in Figure 6 and Figure S13. In dry nitrogen, a clear Ψ signal can be observed down to 0.5 ppm MeOH (Figure S13a), whereas in the presence of 40% relative humidity, the LoD for MeOH is only around 80 ppm (Figure S13c). The same holds for the modeled refractive index (Figure 6a−c). Interestingly, the sensor shows a response to MeOH on top of its response to the 40% relative humidity background. The magnitude of the sensor response to high MeOH concentrations is roughly the same in dry and humidified nitrogen. Exposure to 40% H_2O increases the MOF refractive index by 0.00489 (from 1.35041 to 1.35530). Mixing 8000 ppm MeOH into the humidified N_2 increases n by another 0.00425 (to 1.35955), while 8000 ppm MeOH into dry nitrogen does increase n by 0.00543 (from 1.34961 to 1.35504), i.e., by 0.00118 RIUs (26%) more than in humidified nitrogen. Nevertheless, the MeOH response drops more quickly at lower concentrations in humidified nitrogen compared to dry nitrogen and vanishes at a few tens of ppm (Figure 6f). For the Ψ readout (at one wavelength each), the differences between the measurements in humidified and dry nitrogen are more pronounced (Figure S13a,c). As another example, we studied the LoD of toluene, which is a biomarker for lung cancer.[1] As shown in Figure S14, the refractive index and Ψ responses to vapors in the 1−2 ppm range are 4 and 3 times stronger than for methanol, respectively. Furthermore, an LoD of about 90−100 ppb is observed, which is better than a previously reported plasmonic-based sensor with ZIF-8 (200 ppm)[42] and on par with optical ring-oscillator sensing concepts (76 ppb).[16] At 120 ppb toluene, the SPP/ZIF-8 sensor can still resolve a Δn step of 0.00003.

Finally, it should be pointed out that, although TIRE SPP-based sensing enables resolving changes in the MOF refractive index with a precision of at least 1×10^{-5} (see insets of Figure 6a), it is not possible to derive absolute values without exact knowledge of the thickness t_{MOF} because the SPP λ_r scales linearly with both t_{MOF} and n (Figure 2). Nevertheless, the presented data demonstrate how even very low VOC uptakes can be resolved. Since the same sensitivity is observed not only in the Ψ and Δ of TIRE but also in the intensity of the reflected (p-polarized) light (Figure S15), the realization of practical SPP-based VOC sensors not requiring ellipsometry is feasible. Compared to luminescent sensors based on specific host−guest interactions,[12,43] SPP-based sensing is more versatile because any MOF film with reversible guest adsorption can be applied. Compared to other sensor concepts based on refractive index changes (e.g., DBRs), the deposition of a single MOF thin film is sufficient to realize SPP-based sensors. However, the high sensitivity demonstrated in this work requires not only high-quality MOF thin films but also operation at a well-defined incident angle above the critical angle (to avoid peak broadening upon angular dispersion) as well as application of p-polarized light. Therefore, the realization of SPP-based sensors as a microintegrated optical system is challenging but feasible and might offer a powerful platform for next-generation optical gas sensors and arrays of such devices.[31]

■ CONCLUSIONS

In summary, we have demonstrated the highly sensitive detection of VOCs by transducing their adsorption in MOF thin films into shifts of optically excited SPPs. Resonance peaks as sharp as 14 nm are obtained for ZIF-8 films prepared by MOF-CVD. Upon MeOH adsorption, SPP shifts of up to 160 nm are observed, and a lower limit of detection of <1 ppm is demonstrated. Optical modeling of the measured TIRE/SPP spectra enabled resolving changes in the refractive index with a resolution better than 1×10^{-5}. To achieve this level of performance, the growth and porosity of MOF-CVD ZIF-8 films were systematically studied, with particular attention to the negative impact of film roughness on SPP sharpness and that of linker defects on the VOC uptake. These results can be extended to other VOCs and MOF materials for the development of SPP-based VOC sensor arrays or other integrated optoelectronic gas sensor designs.

■ METHODS

ZIF-8 Thin Film Synthesis and Sample Preparation. A scheme of the Schlenk tube used for MOF-CVD throughout this work is given in Figure S16. Glass substrates (54 mm × 54 mm) were positioned horizontally just below its middle, together with an open vessel containing three to four spatulas (600−800 mg) of 2-mIm linker powder (Sigma-Aldrich, Germany). For sealing the Schlenk tube, a Teflon ring was used so that silicon grease was only needed at the valves. MOF-CVD was performed at 110 °C in a synthesis oven with forced convection (Venti-Line 56 Prime). Prior the reaction, the Schlenk tube was purged through a Schlenk line with dry nitrogen for 7−8 min (except for sample S12; here, only 4 min of purging was used) and finally sealed under nitrogen at 1 atm. Unless stated

otherwise, the MOF films were activated at 110 °C for 2 h in ambient air (convection oven). Silver, AlOx, and ZnO films were RF-sputtered in a Balzers RF-sputter coater (baseline pressure of 2×10^{-5} mbar) at an argon partial pressure of $2-6 \times 10^{-3}$ mbar at 100 W (Ag) or 150 W (oxides). To guarantee homogeneous depositions from sputtering 3 inch targets, the substrates were rotated tangentially over the targets (target−sample distance is 4 cm), which further ensures low deposition rates (ca. 6 nm/min). Two to three substrates were coated simultaneously. The sample-to-sample thickness variation was <0.5 nm. The run-to-run thickness reproducibility was estimated at ±0.5 nm, which is sufficient to enable MOF-CVD films of defined thickness and high porosity.

Spectroscopic Ellipsometry and Total Internal Reflection Ellipsometry. SE and TIRE measurements were performed either with an M-2000X (J. A. Woollam, US; 65° incident angle, spectral range 245−1000 nm) or an iSE (J. A. Woollam, US; 70° incident angle, spectral 400−1000 nm) instrument. The latter was used for the VOC and H_2O vapor exposure experiments (sensing). In these experiments, the samples were placed (together with the prism) in a stainless steel in situ gas cell with glass windows (Thorlabs, UK). For TIRE measurements, the glass substrate (BoroFloat33, n = 1.46953 at 643.8 nm) was positioned on thin support sheets, with the side with the active layers facing downward, and a right-angle prism (Thorlabs, US; 20 mm Cathete lengths, UV fused silica, n = 1.45667 at 644 nm) was attached on top to the substrate backside using glycerol as an n-matching liquid for light in-/out-coupling (cf. Figure 1). Optical modeling was performed using the CompleteEASE (v6) software (J. A. Woollam, US). For the silver films, a B-Spline model was used (cf. Figure S1), whereas for oxide and ZIF-8 films, Cauchy models (C = 0) were applied. In the TIRE configuration, an angle offset of −8.055° (relative to the incident 70°) was fixed. The root mean squared errors (RMSE) for fitting Ψ and Δ spectra in the used TIRE configuration were in the range of 10−20. Nevertheless, the fitted spectra perfectly reproduced the SPP peak position λ_r. For conventional SE measurements, the RMSE for fitting Ψ and Δ spectra were <10, except for thick and rough ZIF-8 films (>15, despite enabling a roughness fit in the Cauchy model). To estimate the uncertainty in the thickness determination, parameter uniqueness fits were performed for the thinnest and thickest ZIF-8 films samples of Figure 3a. The RMSE minimum is less pronounced for the thinner film, which is due to an increased correlation between the refractive index and layer thickness for very thin films. Thus, we estimated that the thickness uncertainty ranges from ±15 to ±5% when going from thin to thick ZIF-8 films (cf. error bars in Figure 3a).

VOC Vapor Supply. VOC vapors were generated via a Bronkhorst Controlled Evaporation Mixing (CEM) system, which consists of a Coriolis liquid flow controller (for methanol and ethanol), a mass flow controller (MFC) for the carrier gas (nitrogen), and a temperature-controlled mixing and evaporation device. The target vapor concentration was set by the ratio of the MFC flows (Bronkhorst Fluidat), yielding VOC vapors with 5−80% p/p^0. Lower concentrations were obtained by diluting vapors with either 5 or 10% p/p^0 (ca. 16,000 ppm for MeOH). Humidified nitrogen was obtained via a bubbler system for water and subsequently mixed with dry nitrogen or/and a diluted dry VOC vapor for generating either N_2:H_2O or N_2:H_2O:VOC vapors of defined concentrations. Home-made LabView programs were used to control the MFCs of the CEM and dilution systems. Typical flows through the in situ cell were in the range of 300−600 sccm. To generate trace concentrations of toluene, a calibrated toluene permeation tube (KIN-TEK Analytical, Inc.) was placed in a permeation oven (Dynacalibrator 150, VICI Metronics. Inc.) held at a precisely controlled temperature of 30.00 °C. Toluene permeates through the tube wall and is released into the nitrogen carrier gas flow. The resulting concentration was calculated as

$$\frac{K \times R(T)}{F}$$

with a constant K = 0.243, the toluene evaporation rate at 30 °C (R(30 °C)) = 285 ng/min, and the nitrogen flow (F) in sccm.

Atomic Force Microscopy. AFM images of 2 μm × 2 μm and 8 μm × 8 μm in size were recorded using an Agilent AFM 5100 microscope with a N2095A/B 9 μm scanner. AC160TS-R3 Olympus microcantilevers were mounted to scan the topography in intermittent contact mode. Using the WSxM 5.0 software,[44] images were processed, and the RMS roughness was calculated as the standard deviation from the average height of the measured height profile of an image. For samples with a high RMS roughness (>30 nm), several images were taken, and the average RMS roughness was determined with deviations of up to a few 10 nm. For samples with ZIF-8 films with thicknesses of <120 nm, this deviation was only a few nm, and hence, only one to two images per sample were taken.

Grazing Incidence X-ray Diffraction. X-ray diffraction data was recorded on a Malvern PANalytical Empyrean diffractometer equipped with a PIXcel3D solid-state detector using a Cu anode (Cu Ka1: 1.5406 Å; Cu Ka2: 1.5444 Å). Before each measurement, an iterative scheme was employed to optimize both sample height (z) and sample tilt (ω). Grazing incidence diffraction patterns were recorded at room temperature in reflection geometry (Bragg−Brentano, incident beam angle 0.2°) within a 5−20° 2θ range using a step size of 0.053° and a counting time of 1000 s per step.

Hard X-ray Photoemission Spectroscopy. Hard X-ray photoemission spectroscopy measurements were performed at IMO-IMOMEC (Hasselt University, Belgium) with a HAXPES lab system (Scienta Omicron, Sweden, Germany) equipped with a liquid gallium jet source (Excillum MetalJet D2; Excillum, Sweden) and a monochromator (HAX9-5; Scienta Omicron) for generating a monochromized (420 meV) Ga K_α beam of $h\nu$ = 9252.4 eV. A 200 mm hemispherical analyzer (R4000, Scienta Omicron) combined with a 40 mm microchannel plate/charge-coupled device detector (MCP/CCD, VG Scienta) with 435 channels was used for photoelectron detection. A slit of 0.8 mm and pass energies of 500 and 200 eV were used for survey and core-level scans, respectively. For the latter, this configuration yields an energy resolution of 590 meV. To verify the correct energy calibration of the instrument under Ga K_α, Au 4f core level scans on a gold reference foil were performed. The hard X-ray beam exiting the monochromator and the analyzer are aligned under a right angle while the sample is tilted by ca. 3° w.r.t. to the incident X-ray beam. The Si/ZIF-8 samples analyzed in this work were synthesized 1 day prior to the transfer into the HAXPES UHV chamber. Before the measurements, the samples were stored in ambient air. To estimate atomic ratios, recently published theoretical elemental photoemission cross sections for Ga K_α excitation were used.[45]

■ AUTHOR INFORMATION

Corresponding Authors

Max L. Tietze − *Centre for Membrane Separations, Adsorption, Catalysis, and Spectroscopy, KU Leuven - University of Leuven, Leuven 3001, Belgium;* orcid.org/0000-0002-9018-3829; Email: maxlutz.tietze@kuleuven.be

Rob Ameloot − *Centre for Membrane Separations, Adsorption, Catalysis, and Spectroscopy, KU Leuven - University of Leuven, Leuven 3001, Belgium;* orcid.org/0000-0003-3178-5480; Email: rob.ameloot@kuleuven.be

Authors

Martin Obst − *Centre for Membrane Separations, Adsorption, Catalysis, and Spectroscopy, KU Leuven - University of Leuven, Leuven 3001, Belgium*

Giel Arnauts − *Centre for Membrane Separations, Adsorption, Catalysis, and Spectroscopy, KU Leuven - University of Leuven, Leuven 3001, Belgium*

Nathalie Wauteraerts − *Centre for Membrane Separations, Adsorption, Catalysis, and Spectroscopy, KU Leuven - University of Leuven, Leuven 3001, Belgium*

Sabina Rodríguez-Hermida − *Centre for Membrane Separations, Adsorption, Catalysis, and Spectroscopy, KU Leuven - University of Leuven, Leuven 3001, Belgium*

Author Contributions

The manuscript was written through contributions of all authors.

All authors have given approval to the final version of the manuscript.

Funding

M.L.T. acknowledges financial support from the Research Foundation Flanders (FWO) by a senior postdoctoral fellowship (12ZK720N). N.W. and G.A. acknowledge financial support from the FWO by SB-PhD fellowships (1SB7919N and 1SA7320N). R.A. acknowledges funding from the European Research Council (no. 716472, VAPORE) and the FWO for funding in the large-scale infrastructure project HERCULES HAXPES (I014018N).

Notes

The authors declare no competing financial interest.

■ ACKNOWLEDGMENTS

The authors thank J. Marreiros and A. J. Cruz for fruitful discussions.

■ ABBREVIATIONS

MOF, metal−organic framework
TIRE, total internal reflection ellipsometry
SPP, surface plasmon polariton
SE, spectroscopic ellipsometry
EP, ellipsometric porosimetry
ZIF-8, zeolitic imidazolate framework 8

■ REFERENCES

(1) Peng, G.; Tisch, U.; Adams, O.; Hakim, M.; Shehada, N.; Broza, Y. Y.; Billan, S.; Abdah-Bortnyak, R.; Kuten, A.; Haick, H. Diagnosing Lung Cancer in Exhaled Breath Using Gold Nanoparticles. *Nat. Nanotechnol.* **2009**, *4*, 669−673.

(2) Righettoni, M.; Tricoli, A.; Gass, S.; Schmid, A.; Amann, A.; Pratsinis, S. E. Breath Acetone Monitoring by Portable Si:WO3 Gas Sensors. *Anal. Chim. Acta* **2012**, *738*, 69−75.

(3) Lewis, A.; Edwards, P. Validate Personal Air-Pollution Sensors. *Nature* **2016**, *535*, 29.

(4) Malik, R.; Tomer, V. K.; Mishra, Y. K.; Lin, L. Functional Gas Sensing Nanomaterials: A Panoramic View. *Appl. Phys. Rev.* **2020**, *7*, No. 021301.

(5) Hwang, K.; Ahn, J.; Cho, I.; Kang, K.; Kim, K.; Choi, J.; Polychronopoulou, K.; Park, I. Microporous Elastomer Filter Coated with Metal Organic Frameworks for Improved Selectivity and Stability of Metal Oxide Gas Sensors. *ACS Appl. Mater. Interfaces* **2020**, *12*, 13338−13347.

(6) Caro, J. Quo Vadis, MOF? *Chem. Ing. Tech.* **2018**, *90*, 1759−1768.

(7) Stassen, I.; Burtch, N.; Talin, A.; Falcaro, P.; Allendorf, M.; Ameloot, R. An Updated Roadmap for the Integration of Metal−Organic Frameworks with Electronic Devices and Chemical Sensors. *Chem. Soc. Rev.* **2017**, *46*, 3185−3241.

(8) Tchalala, M. R.; Bhatt, P. M.; Chappanda, K. N.; Tavares, S. R.; Adil, K.; Belmabkhout, Y.; Shkurenko, A.; Cadiau, A.; Heymans, N.; De Weireld, G.; Maurin, G.; Salama, K. N.; Eddaoudi, M. Fluorinated MOF Platform for Selective Removal and Sensing of SO2 from Flue Gas and Air. *Nat. Commun.* **2019**, *10*, 1−10.

(9) Zhang, K.; Lively, R. P.; Dose, M. E.; Brown, A. J.; Zhang, C.; Chung, J.; Nair, S.; Koros, W. J.; Chance, R. R. Alcohol and Water Adsorption in Zeolitic Imidazolate Frameworks. *Chem. Commun.* **2013**, *49*, 3245.

(10) Freund, R.; Zaremba, O.; Arnauts, G.; Ameloot, R.; Skorupskii, G.; Dincă, M.; Bavykina, A.; Gascon, J.; Ejsmont, A.; Gościańska, J.; Kalmutzki, M.; Lächelt, U.; Ploetz, E.; Diercks, C.; Wuttke, S. The Current Status of MOF and COF Applications. *Angew. Chem. Int. Ed.* **2021**, *60*, 23975.

(11) Chui, S. S.-Y.; Lo, S. M.-F.; Charmant, J. P. H.; Orpen, A. G.; Williams, I. D. A Chemically Functionalizable Nanoporous Material [Cu3(TMA)2(H2O)3]n. *Science* **1999**, *283*, 1148−1150.

(12) Takashima, Y.; Martínez, V. M.; Furukawa, S.; Kondo, M.; Shimomura, S.; Uehara, H.; Nakahama, M.; Sugimoto, K.; Kitagawa, S. Molecular Decoding Using Luminescence from an Entangled Porous Framework. *Nat. Commun.* **2011**, *2*, 168.

(13) Redel, E.; Wang, Z.; Walheim, S.; Liu, J.; Gliemann, H.; Wöll, C. On the Dielectric and Optical Properties of Surface-Anchored Metal-Organic Frameworks: A Study on Epitaxially Grown Thin Films. *Appl. Phys. Lett.* **2013**, *103*, No. 091903.

(14) Demessence, A.; Horcajada, P.; Serre, C.; Boissière, C.; Grosso, D.; Sanchez, C.; Férey, G. Elaboration and Properties of Hierarchically Structured Optical Thin Films of MIL-101(Cr). *Chem. Commun.* **2009**, *46*, 7149−7151.

(15) Lu, G.; Hupp, J. T. Metal−Organic Frameworks as Sensors: A ZIF-8 Based Fabry−Pérot Device as a Selective Sensor for Chemical Vapors and Gases. *J. Am. Chem. Soc.* **2010**, *132*, 7832−7833.

(16) Tao, J.; Wang, X.; Sun, T.; Cai, H.; Wang, Y.; Lin, T.; Fu, D.; Ting, L. L. Y.; Gu, Y.; Zhao, D. Hybrid Photonic Cavity with Metal-Organic Framework Coatings for the Ultra-Sensitive Detection of Volatile Organic Compounds with High Immunity to Humidity. *Sci. Rep.* **2017**, *7*, 1−8.

(17) Li, C.; Li, L.; Yu, S.; Jiao, X.; Chen, D. High Performance Hollow Metal−Organic Framework Nanoshell-Based Etalons for Volatile Organic Compounds Detection. *Adv. Mater. Technol.* **2016**, *1*, 1600127.

(18) Liu, J.; Redel, E.; Walheim, S.; Wang, Z.; Oberst, V.; Liu, J.; Heissler, S.; Welle, A.; Moosmann, M.; Scherer, T.; Bruns, M.; Gliemann, H.; Wöll, C. Monolithic High Performance Surface Anchored Metal−Organic Framework Bragg Reflector for Optical Sensing. *Chem. Mater.* **2015**, *27*, 1991−1996.

(19) von Mankowski, A.; Szendrei-Temesi, K.; Koschnick, C.; Lotsch, B. V. Improving Analyte Selectivity by Post-Assembly Modification of Metal−Organic Framework Based Photonic Crystal Sensors. *Nanoscale Horiz.* **2018**, *3*, 383−390.

(20) Ranft, A.; Niekiel, F.; Pavlichenko, I.; Stock, N.; Lotsch, B. V. Tandem MOF-Based Photonic Crystals for Enhanced Analyte-Specific Optical Detection. *Chem. Mater.* **2015**, *27*, 1961−1970.

(21) Xing, Y.; Shi, L.; Yan, J.; Chen, Y. High-Performance Methanal Sensor Based on Metal-Organic Framework Based One-Dimensional Photonic Crystal. *ChemistrySelect* **2020**, *5*, 3946−3952.

(22) Hinterholzinger, F. M.; Ranft, A.; Feckl, J. M.; Rühle, B.; Bein, T.; Lotsch, B. V. One-Dimensional Metal−Organic Framework

Photonic Crystals Used as Platforms for Vapor Sorption. *J. Mater. Chem.* **2012**, *22*, 10356−10362.
(23) Avci, C.; Imaz, I.; Carné-Sánchez, A.; Pariente, J. A.; Tasios, N.; Pérez-Carvajal, J.; Alonso, M. I.; Blanco, A.; Dijkstra, M.; López, C.; Maspoch, D. Self-Assembly of Polyhedral Metal−Organic Framework Particles into Three-Dimensional Ordered Superstructures. *Nat. Chem.* **2018**, *10*, 78−84.
(24) Kreno, L. E.; Hupp, J. T.; Van Duyne, R. P. Metal−Organic Framework Thin Film for Enhanced Localized Surface Plasmon Resonance Gas Sensing. *Anal. Chem.* **2010**, *82*, 8042−8046.
(25) Miliutina, E.; Guselnikova, O.; Chufistova, S.; Kolska, Z.; Elashnikov, R.; Burtsev, V.; Postnikov, P.; Svorcik, V.; Lyutakov, O. Fast and All-Optical Hydrogen Sensor Based on Gold-Coated Optical Fiber Functionalized with Metal−Organic Framework Layer. *ACS Sens.* **2019**, *4*, 3133−3140.
(26) Hromadka, J.; Tokay, B.; Correia, R.; Morgan, S. P.; Korposh, S. Highly Sensitive Volatile Organic Compounds Vapour Measurements Using a Long Period Grating Optical Fibre Sensor Coated with Metal Organic Framework ZIF-8. *Sens. Actuators, B* **2018**, *260*, 685−692.
(27) Tu, M.; Wannapaiboon, S.; Khaletskaya, K.; Fischer, R. A. Engineering Zeolitic-Imidazolate Framework (ZIF) Thin Film Devices for Selective Detection of Volatile Organic Compounds. *Adv. Funct. Mater.* **2015**, *25*, 4470−4479.
(28) Stassen, I.; Styles, M.; Grenci, G.; Gorp, H. V.; Vanderlinden, W.; Feyter, S. D.; Falcaro, P.; Vos, D. D.; Vereecken, P.; Ameloot, R. Chemical Vapour Deposition of Zeolitic Imidazolate Framework Thin Films. *Nat. Mater.* **2016**, *15*, 304−310.
(29) Arwin, H. TIRE and SPR-Enhanced SE for Adsorption Processes. In *Ellipsometry of Functional Organic Surfaces and Films*; Hinrichs, K., Eichhorn, K.-J., Eds.; Springer Series in Surface Sciences; Springer International Publishing: Cham: 2018, pp. 419−435, DOI: 10.1007/978-3-319-75895-4_18.
(30) Nabok, A.; Tsargorodskaya, A. The Method of Total Internal Reflection Ellipsometry for Thin Film Characterisation and Sensing. *Thin Solid Films* **2008**, *516*, 8993−9001.
(31) Brenet, S.; John-Herpin, A.; Gallat, F.-X.; Musnier, B.; Buhot, A.; Herrier, C.; Rousselle, T.; Livache, T.; Hou, Y. Highly-Selective Optoelectronic Nose Based on Surface Plasmon Resonance Imaging for Sensing Volatile Organic Compounds. *Anal. Chem.* **2018**, *90*, 9879−9887.
(32) Woollam, J. A.; Johs, B. D.; Herzinger, C. M.; Hilfiker, J. N.; Synowicki, R. A.; Bungay, C. L. Overview of Variable-Angle Spectroscopic Ellipsometry (VASE): I. Basic Theory and Typical Applications. *Optical Metrology: A Critical Review*; International Society for Optics and Photonics: Bellingham, United States, 1999; p 1029402, DOI: 10.1117/12.351660.
(33) Zayats, A. V.; Smolyaninov, I. I.; Maradudin, A. A. Nano-Optics of Surface Plasmon Polaritons. *Phys. Rep.* **2005**, *408*, 131−314.
(34) Grau-Crespo, R.; Aziz, A.; Collins, A. W.; Crespo-Otero, R.; Hernández, N. C.; Rodriguez-Albelo, L. M.; Ruiz-Salvador, A. R.; Calero, S.; Hamad, S. Modelling a Linker Mix-and-Match Approach for Controlling the Optical Excitation Gaps and Band Alignment of Zeolitic Imidazolate Frameworks. *Angew. Chem., Int. Ed.* **2016**, *55*, 16012−16016.
(35) Cruz, A. J.; Stassen, I.; Krishtab, M.; Marcoen, K.; Stassin, T.; Rodríguez-Hermida, S.; Teyssandier, J.; Pletincx, S.; Verbeke, R.; Rubio-Giménez, V.; Tatay, S.; Martí-Gastaldo, C.; Meersschaut, J.; Vereecken, P. M.; De Feyter, S.; Hauffman, T.; Ameloot, R. Integrated Cleanroom Process for the Vapor-Phase Deposition of Large-Area Zeolitic Imidazolate Framework Thin Films. *Chem. Mater.* **2019**, *31*, 9462−9471.
(36) Bux, H.; Feldhoff, A.; Cravillon, J.; Wiebcke, M.; Li, Y.-S.; Caro, J. Oriented Zeolitic Imidazolate Framework-8 Membrane with Sharp H2/C3H8 Molecular Sieve Separation. *Chem. Mater.* **2011**, *23*, 2262−2269.
(37) Navarro, M.; Seoane, B.; Mateo, E.; Lahoz, R.; de la Fuente, G. F.; Coronas, J. ZIF-8 Micromembranes for Gas Separation Prepared on Laser-Perforated Brass Supports. *J. Mater. Chem. A* **2014**, *2*, 11177−11184.
(38) Katsenis, A. D.; Puškarić, A.; Štrukil, V.; Mottillo, C.; Julien, P. A.; Užarević, K.; Pham, M.-H.; Do, T.-O.; Kimber, S. A. J.; Lazić, P.; Magdysyuk, O.; Dinnebier, R. E.; Halasz, I.; Friščić, T. In Situ X-Ray Diffraction Monitoring of a Mechanochemical Reaction Reveals a Unique Topology Metal-Organic Framework. *Nat. Commun.* **2015**, *6*, 6662.
(39) Regoutz, A.; Mascheck, M.; Wiell, T.; Eriksson, S. K.; Liljenberg, C.; Tetzner, K.; Williamson, B. A. D.; Scanlon, D. O.; Palmgren, P. A Novel Laboratory-Based Hard X-Ray Photoelectron Spectroscopy System. *Rev. Sci. Instrum.* **2018**, *89*, No. 073105.
(40) Zhang, C.; Han, C.; Sholl, D. S.; Schmidt, J. R. Computational Characterization of Defects in Metal−Organic Frameworks: Spontaneous and Water-Induced Point Defects in ZIF-8. *J. Phys. Chem. Lett.* **2016**, *7*, 459−464.
(41) Winiarski, J.; Tylus, W.; Winiarska, K.; Szczygieł, I.; Szczygieł, B. XPS and FT-IR Characterization of Selected Synthetic Corrosion Products of Zinc Expected in Neutral Environment Containing Chloride Ions. *Journal of Spectroscopy* **2018**, *2018*, 1.
(42) Koh, C. S. L.; Lee, H. K.; Han, X.; Sim, H. Y. F.; Ling, X. Y. Plasmonic Nose: Integrating the MOF-Enabled Molecular Preconcentration Effect with a Plasmonic Array for Recognition of Molecular-Level Volatile Organic Compounds. *Chem. Commun.* **2018**, *54*, 2546−2549.
(43) Allendorf, M. D.; Bauer, C. A.; Bhakta, R. K.; Houk, R. J. T. Luminescent Metal−Organic Frameworks. *Chem. Soc. Rev.* **2009**, *38*, 1330−1352.
(44) Horcas, I.; Fernández, R.; Gómez-Rodríguez, J. M.; Colchero, J.; Gómez-Herrero, J.; Baro, A. M. WSXM: A Software for Scanning Probe Microscopy and a Tool for Nanotechnology. *Rev. Sci. Instrum.* **2007**, *78*, No. 013705.
(45) Trzhaskovskaya, M. B.; Yarzhemsky, V. G. Dirac−Fock Photoionization Parameters for HAXPES Applications. *At. Data Nucl. Data Tables* **2018**, *119*, 99−174.
(46) Mottillo, C.; Friscic, T. Carbon Dioxide Sensitivity of Zeolitic Imidazolate Frameworks. *Angew. Chem. Int. Ed.* **2014**, *53*, 7471−7474.